


Quantum Magnetism and Topological Superconductivity in Yu-Shiba-Rusinov Chains

Jacob F. Steiner¹,[✉] Christophe Mora,^{1,2} Katharina J. Franke³,[✉] and Felix von Oppen¹

¹*Dahlem Center for Complex Quantum Systems and Fachbereich Physik, Freie Universität Berlin, 14195 Berlin, Germany*

²*Laboratoire Matériaux et Phénomènes Quantiques, CNRS, Université de Paris, 75013 Paris, France*

³*Fachbereich Physik, Freie Universität Berlin, 14195 Berlin, Germany*

 (Received 4 June 2021; revised 2 November 2021; accepted 7 January 2022; published 21 January 2022)

Chains of magnetic adatoms on superconductors have been discussed as promising systems for realizing Majorana end states. Here, we show that dilute Yu-Shiba-Rusinov (YSR) chains are also a versatile platform for quantum magnetism and correlated electron dynamics, with widely adjustable spin values and couplings. Focusing on subgap excitations, we derive an extended $t - J$ model for dilute quantum YSR chains and use it to study the phase diagram as well as tunneling spectra. We explore the implications of quantum magnetism for the formation of a topological superconducting phase, contrasting it to existing models assuming classical spin textures.

DOI: [10.1103/PhysRevLett.128.036801](https://doi.org/10.1103/PhysRevLett.128.036801)

Introduction.—Dilute chains of magnetic adatoms on superconductors have been proposed as a possible setting for topological superconductivity [1–6], complementing the frequently studied densely packed chains [7–12]. While the latter are dominated by direct hybridization of adatom d orbitals [13,14], the former couple adatoms only indirectly via the substrate provided that the adatoms are spaced close enough that their Yu-Shiba-Rusinov (YSR) states [15–18] overlap. Theoretical models assume that the Ruderman-Kittel-Kasuya-Yosida (RKKY) interaction, possibly aided by magnetic anisotropy, induce ordered magnetic textures, which are then described as chains of classical spins [1,2,19–26].

Contrasting with classical spin models, observations of Kondo resonances and discrete spin excitations imply that individual adatom spins behave quantum mechanically, both on normal and on superconducting substrates [27–30]. Here, we show that the quantum nature of adatom spins makes dilute chains an intriguing experimental platform beyond Majorana physics, displaying rich correlated-electron physics as reflected in qualitatively different phase diagrams and excitation spectra. This is a consequence of quantum phase transitions [31,32], which change the effective spin due to screening by bound quasiparticles [30,33,34], a phenomenon specific to quantum spins and absent for classical spins.

We find that signatures of the quantum spin nature are directly observable in local excitation spectra of adatom chains, as probed, for instance, by scanning tunneling spectroscopy. Moreover, the topological superconducting phase exhibiting Majorana states can be dramatically reduced in parameter space compared to classical models. The effective spin as well as magnitude and sign of the RKKY coupling between impurity spins can, in principle, be adjusted. In real materials, magnetic anisotropy,

Dzyaloshinskii-Moriya (DM) interactions, and spin-orbit coupled substrate electrons further enrich the physics of these quantum spin chains.

The correlated-electron physics of dilute adatom chains is due to correlated spin-fermion dynamics, which we find to be described by an extension of the $t - J$ model [35], admitting topological superconductivity for ferromagnetic and spin-charge separation for antiferromagnetic RKKY coupling. For a theoretical treatment of quantum chains, we project out the quasiparticle continuum of the superconductor in the limit of a large pairing gap and retain only the subgap YSR excitations induced by the magnetic adatoms. The resulting model includes a single superconducting site per adatom (and conduction-electron channel), so that Kondo renormalizations must be accounted for separately. Despite its simplicity, the model qualitatively reproduces [32] phase diagrams and excitation spectra of individual higher-spin impurities subject to single-ion anisotropy [36] and spin- $\frac{1}{2}$ dimers [37,38] obtained from the numerical renormalization group.

Model.—We therefore extend this approach to quantum chains of spin- S adatoms. For a single YSR excitation per adatom, the model takes the form

$$H = \sum_j \{ \Delta (c_{j\uparrow}^\dagger c_{j\downarrow}^\dagger + \text{H.c.}) + c_{j\sigma}^\dagger [V\delta_{\sigma\sigma'} + \mathbf{S}_j \cdot \mathbf{K} \cdot \mathbf{s}_{\sigma\sigma'}] c_{j\sigma'} - t [c_{j\sigma}^\dagger c_{j+1,\sigma} + \text{H.c.}] + \mathbf{S}_j \cdot \mathbf{J} \cdot \mathbf{S}_{j+1} + D(S_j^z)^2 \}, \quad (1)$$

where j enumerates the adatoms along the chain and sums over repeated spin indices σ, σ' are implied. At each site j , the conduction electrons (creation operator $c_{j\sigma}^\dagger$, spin- $\frac{1}{2}$ matrices \mathbf{s}) couple to the local impurity spin \mathbf{S}_j via antiferromagnetic exchange K and potential scattering V . The hopping t between adjacent superconducting sites

(pairing strength Δ) models the hybridization of YSR states. The quasiparticle continuum of the substrate mediates an interaction J between nearest-neighbor adatom spins, incorporating both the RKKY (symmetric part) and the DM interaction (antisymmetric part) [38]. We also include single-ion anisotropy D relevant for $S \geq 1$. In general, magnetic adatoms induce YSR states in multiple conduction-electron channels. This could be included in Eq. (1) by coupling each impurity spin to multiple superconducting sites [32].

Spin- $\frac{1}{2}$ impurities.—We exemplify the physics of dilute quantum YSR chains by spin- $\frac{1}{2}$ adatoms. The individual impurities undergo a quantum phase transition with increasing exchange coupling K [18,31,32]. At weak coupling, the conduction electrons are fully paired (even fermion parity), leaving an unscreened (free) impurity spin and a doubly degenerate ground state. Within the single-site model, the doublet ground state (energy E_{BCS}) takes the form $|\pm\rangle = |S^z = \uparrow/\downarrow\rangle \otimes |\text{BCS}\rangle$, where $|\text{BCS}\rangle = (u + v c_{\downarrow}^{\dagger} c_{\uparrow}^{\dagger})|\text{vac}\rangle$ is the paired BCS state. At strong coupling, the impurity forms a singlet with the conduction electrons by binding a quasiparticle (odd fermion parity). The resulting screened-spin ground state (energy E_0) is nondegenerate and takes the form $|0\rangle = (1/\sqrt{2})(|\uparrow\downarrow\rangle - |\downarrow\uparrow\rangle)$. The transition between these ground states occurs when the energy of the YSR excitation $E_{\text{YSR}} = E_0 - E_{\text{BCS}}$ changes sign (see Supplemental Material [39] for details, including explicit expressions for u , v , and E_{YSR}).

Whereas, for quantum spins, the quantum phase transition is associated with screening of the adatom spin due to the singlet formation, screening is absent in classical spin models [39]. This difference has important ramifications in dilute chains. When coupling adatoms in the unscreened state (E_{YSR} large and positive) into a dilute chain, they form a quantum spin-1/2 chain subject to RKKY interactions. The YSR excitation of one of the adatoms into the screened state, e.g., by tunneling from a STM tip, quenches its spin and breaks the adjacent RKKY bonds. The quenched spin is mobile along the chain due to the hybridization of YSR states and propagates in a correlated spin background. In contrast, there is only a single low-energy state when coupling impurities in the screened state (E_{YSR} large and negative). The YSR excitation of an adatom into the free-spin state introduces one free spin, which propagates in a (largely) spin-free background. For intermediate values of $|E_{\text{YSR}}|$, the impurity spins may neither be all free (no bound quasiparticles) nor all screened (N bound quasiparticles). However, the adatom chain gains RKKY energy only when coupling unscreened adatoms, so that RKKY coupling favors the fully unscreened phase. This causes dramatic differences between the phase diagrams of chains of classical and quantum spins.

Extended $t - J$ model.—We explore the phase diagram by exact diagonalization complemented by analytical

considerations. We eliminate the above-gap states (which are unphysical in our model) and retain only the fully paired states $|\pm\rangle$ and the singlet $|0\rangle$ of each site by considering $\Delta, K, V \gg E_{\text{YSR}}, t, J$. In this limit, Eq. (1) projects to an extended $t - J$ model. Regarding the local singlets $|0\rangle$ as the vacuum and introducing a spinful fermion d_{σ} for each site through $|\pm\rangle = d_{\pm}^{\dagger}|0\rangle$ and $d_{\pm}|0\rangle = 0$, we find [40]

$$H_{IJ} = \mathcal{P} \sum_j \{ -E_{\text{YSR}} n_j + \mathbf{S}_j \cdot \mathbf{J} \cdot \mathbf{S}_{j+1} - [\tilde{t} d_{j,\sigma}^{\dagger} d_{j+1,\sigma} + \tilde{\Delta} (d_{j,\uparrow}^{\dagger} d_{j+1,\downarrow}^{\dagger} - d_{j,\downarrow}^{\dagger} d_{j+1,\uparrow}^{\dagger}) + \text{H.c.}] \} \mathcal{P}. \quad (2)$$

As in the $t - J$ model, the projection to the physical subspace that excludes doubly occupied sites is implemented by the projector \mathcal{P} . Here, $n_j = \sum_{\sigma} n_{j,\sigma} = \sum_{\sigma} d_{j,\sigma}^{\dagger} d_{j,\sigma}$, the spin operators $\mathbf{S}_j = \sum_{\sigma\sigma'} d_{j,\sigma}^{\dagger} \mathbf{s}_{\sigma\sigma'} d_{j,\sigma'}$ are now associated with the d fermions, and the effective hopping and pairing amplitudes are $\tilde{t} = tV/(2\sqrt{\Delta^2 + V^2})$ and $\tilde{\Delta} = t\Delta/(2\sqrt{\Delta^2 + V^2})$ [39]. These originate from conduction electrons hopping between adjacent sites (amplitude t) as illustrated in Fig. 1(a). Hopping between a screened and a free-spin site effectively moves the free spin (amplitude \tilde{t}) and thus the d fermion. Hopping between two free-spin sites screens them (or vice versa), annihilating (creating) a d -fermion pair and inducing pairing (amplitude $\tilde{\Delta}$). Finally, E_{YSR} acts as a chemical potential for the d fermions. We note that the Hamiltonian in Eq. (2) conserves fermion parity and total spin (for isotropic J), but not fermion number.

The phase diagram as a function of E_{YSR} and the (isotropic) RKKY interaction J can be inferred from the expectation value of the number of holes (sites with screened impurity spin) $n_{\text{holes}} = N - \sum_j n_j$, as well as the total spin S_{tot} in the ground state. Figure 1(b) shows corresponding exact-diagonalization results for a chain of $N = 10$ impurity spins with periodic boundary conditions. For sufficiently large $E_{\text{YSR}} > 0$, the chain has no holes and realizes a spin- $\frac{1}{2}$ Heisenberg chain. As E_{YSR} is reduced, the number of holes increases and eventually becomes equal to N . In this state, all impurity spins are screened and the ground state has $S_{\text{tot}} = 0$.

Figure 1(c) shows a corresponding phase diagram for a chain of classical spins for contrast (see Supplemental Material [39] for more details). The classical phase diagram reflects filling of a YSR band. The YSR bands emerge from the positive- and negative-energy YSR states (band energies $\pm E_{\text{YSR}} - (\Lambda/2) < \epsilon < \pm E_{\text{YSR}} + (\Lambda/2)$) and overlap when $-(\Lambda/2) < E_{\text{YSR}} < (\Lambda/2)$. As E_{YSR} decreases from $(\Lambda/2)$ to $-(\Lambda/2)$, the number of holes n_{holes} increases continuously from 0 to N . Here, the bandwidth Λ depends only on the sign, but not on the magnitude of the RKKY coupling.

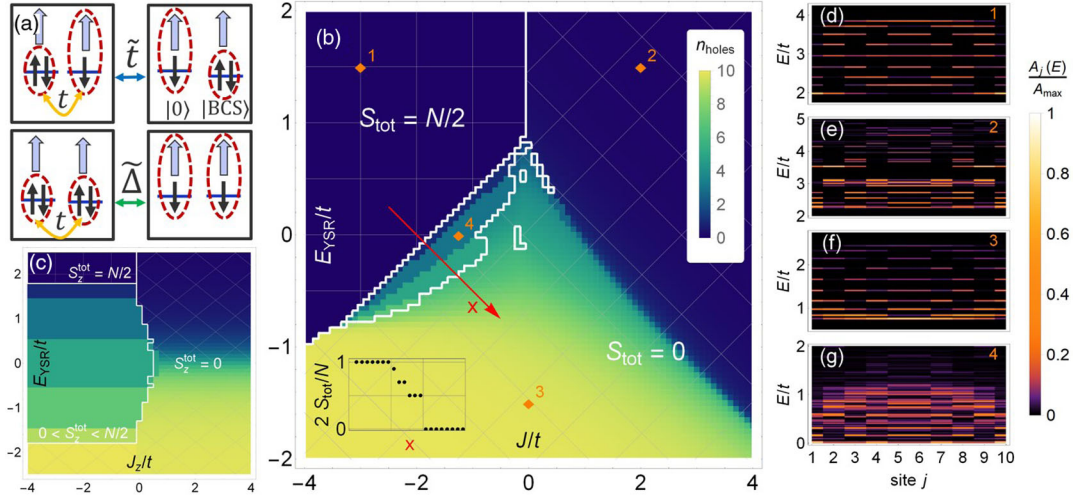


FIG. 1. (a) Processes underlying effective hopping (\tilde{t}) and pairing ($\tilde{\Delta}$) of extended $t - J$ model. (b)–(g) Exact-diagonalization results for a chain of $N = 10$ impurity spins ($V = 2\Delta$; $\tilde{t} = 2\tilde{\Delta}$). (b) Phase diagram for a (periodic) chain of quantum spins (with isotropic K) as a function of YSR energy E_{YSR} and isotropic RKKY interaction J , based on the number of holes (screened spins) n_{holes} (color scale) and total spin S_{tot} . White lines delineate borders of maximal (minimal) spin phases, which are indicated by horizontal (tilted) mesh. Regions without mesh have intermediate S_{tot} . (c) Corresponding phase diagram for a classical chain (see Supplemental Material [39] for details). (d)–(g) Site-resolved single-particle spectral functions of a quantum chain with open boundary conditions for (d) $(E_{\text{YSR}}, J) = (1.5, -3)$, (e) $(1.5, 2)$, (f) $(-1.5, 0)$, (g) $(0, -1.25)$. Panel numbers in (d)–(g) refer to numbered diamonds in (b).

This contrasts starkly with the strong J dependence of the phase boundaries for quantum spins. For quantum spins, the RKKY energy contributes only for unscreened spins, so that the Heisenberg phases in which all spins are unscreened are stabilized by increasing $|J|$. The physics is reminiscent of the classical picture only near $J = 0$ [41], where n_{holes} varies from 0 to N for $|E_{\text{YSR}}| \lesssim 2\tilde{t}$ [green region in Fig. 1(b)]. On the antiferromagnetic side ($J > 0$), the width of the shifted transition region [green in Fig. 1(b)] narrows, saturating for larger J . While increasing antiferromagnetic correlations suppress the effect of hopping \tilde{t} , the spin-singlet pairing $\tilde{\Delta}$ introduces an uncertainty in n_{holes} , which eventually governs the width of the transition region. At the same time, the total spin of the ground state is $S_{\text{tot}} = 0$, regardless of E_{YSR} . As E_{YSR} is reduced, the ground state changes from a total singlet formed by antiferromagnetically coupled impurity spins to a chain of local singlets between impurity spins and conduction electrons.

On the ferromagnetic side ($J < 0$), the transition region rapidly narrows as $|J|$ increases, ultimately giving way to a direct phase boundary between the Heisenberg spin chain and fully screened state. This transition is largely insensitive to the spin-singlet pairing $\tilde{\Delta}$ due to the strong spin polarization. Reducing E_{YSR} at smaller $|J|$ eventually introduces holes into the Heisenberg ferromagnet, and the system becomes a metallic ferromagnet. A stepwise increase in the number of holes prompts a corresponding reduction of the total spin S_{tot} from its maximum of $N/2$ [inset in Fig. 1(b)]. Although this is similar to the classical scenario, S_{tot} jumps discontinuously to zero before the

number of holes reaches N . Here, the metallic ferromagnet becomes energetically less favorable than a superconducting phase favored by the spin-singlet pairing $\tilde{\Delta}$. This singlet superconductor has $S_{\text{tot}} = 0$, as do the Heisenberg antiferromagnet and the local-singlet phase at large and negative E_{YSR} . The fine structure of the phase boundaries in Fig. 1(b) reflects finite-size effects related to the infinite- U Hubbard model, see [39,42].

Pronounced differences from the classical scenario also appear in the site-resolved single-particle spectral function, which directly reveal strong correlations and are accessible by scanning tunneling microscopy [43]. Corresponding exact-diagonalization data for a chain of $N = 10$ impurity spins with open boundary conditions are shown in Figs. 1(d)–1(g). (Corresponding results for classical spins are shown in the Supplemental Material [39].) Probing the Heisenberg spin chain (sufficiently large $E_{\text{YSR}} > 0$), the YSR excitation of one of the impurities screens its spin and induces a mobile hole. In the ferromagnetic phase [Fig. 1(d)], the excited hole perturbs the spin background only weakly and to a good approximation, its motion is described by a tight-binding chain. Correspondingly, in the lower (upper) half of the hole band, i.e., $2 \lesssim E/t \lesssim 3$ ($3 \lesssim E/t \lesssim 4$), the number of nodes in the spectral function increases (decreases) with energy. Moreover, there is enhanced (reduced) intensity at the ends, since a hole on a boundary site breaks only one rather than two ferromagnetic bonds, inducing a lower site energy. (We note that, at finite energy resolution and a small excitation gap, this effect may lead to similar experimental phenomenology as a Majorana.) In the antiferromagnetic phase

[Fig. 1(e)], in contrast, the spectral weight spreads over many more many-body states due to the spin-charge separation in the antiferromagnetic $t - J$ model.

For a chain of fully screened impurity spins [Fig. 1(f)], the YSR excitation unscreens one of the impurity spins. To lowest order, the spectral function can again be understood in terms of a tight-binding band describing the mobile spin, now with uniform site energies throughout the chain. However, unlike in the ferromagnetic phase, the number of spins is no longer a good quantum number due to the effective pairing. The associated redistribution of spectral weight to states with additional spins leads to a reduction in intensity of the single-particle-like spectral peaks with increasing excitation energy.

The metallic ferromagnet has strong similarities with the regime of overlapping YSR bands for classical ferromagnetic textures in the absence of spin-orbit coupling. In particular, it has a gapless excitation spectrum [Fig. 1(g)]. The spectral function exhibits several nodes even at the lowest energy, as holes are already present in the ground state, and becomes dense at higher energies due to the coupling to the particle-hole continuum.

The metallic ferromagnet can become a topological superconductor for spin-orbit coupled superconductors. Spin-orbit coupling makes the YSR hybridization spin dependent and breaks spin-rotation symmetry. Specifically, we introduce spin-dependent hopping $-t \sum_j c_j^\dagger (1 + i\alpha\sigma_y) c_{j+1} + \text{H.c.}$ and anisotropic (Ising-like) RKKY interactions $J_z \sum_j S_j^z S_{j+1}^z$ polarized perpendicular to the spin-orbit field. Without double-occupation constraint, Ref. [44] studied this model as a paradigm for the interplay of topological superconductivity and interactions.

Corresponding numerical results are shown in Fig. 2 for a chain of $N = 12$ sites with open boundary conditions. Without spin-orbit coupling, the phase diagram (see Supplemental Material [39]) is qualitatively similar to Fig. 1(b) for Heisenberg interactions. Spin-orbit coupling only weakly affects the ferromagnetic insulator at $J_z/t \lesssim -1.8$ or the singlet superconductor at $J_z/t \gtrsim -0.7$, but the spectrum of the metallic ferromagnet ($-1.8 \lesssim J_z/t \lesssim -0.7$) develops a p -wave pairing gap [Fig. 2(a)]. The associated formation of Majorana end states leads to four (up to finite-size corrections) degenerate ground states, a pair of even- and odd-fermion-parity states for each of the two symmetry-broken spin configurations. In line with a topological degeneracy, even- and odd-parity ground states are indistinguishable by the local observables n_{holes} and the total spin projection S_{tot}^z [Fig. 2(b)]. For sufficiently large $|J|$, the p -wave gap [Fig. 2(a)] as well as n_{holes} and S_{tot}^z [Fig. 2(b)] can be well reproduced analytically, using a variational trial state for the metallic ferromagnet and including the spin-orbit coupling into the extended $t - J$ model (see [39] for theoretical details). At smaller $|J|$, the analytical description breaks down as it neglects the effects of the singlet pairing $\tilde{\Delta}$. Tunneling spectra clearly reveal the formation of

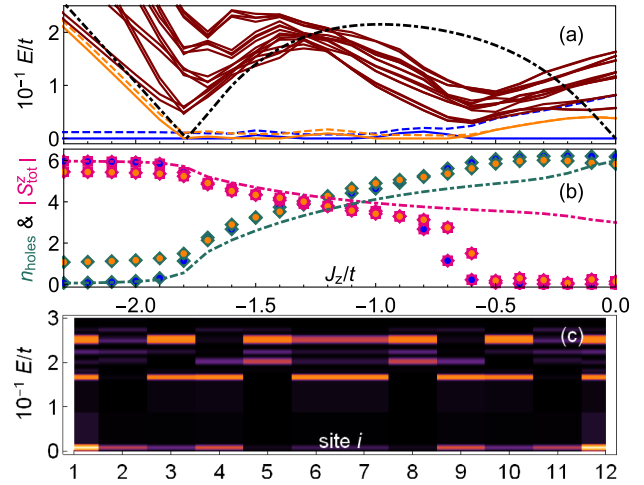


FIG. 2. Exact-diagonalization results for $N = 12$ chain with Ising RKKY interaction and spin-orbit coupling. (a) Ten lowest-energy eigenstates each vs RKKY coupling J_z in even- and odd-parity sectors at $E_{\text{YSR}} = 0$, cutting through the metallic ferromagnet for zero spin-orbit coupling (for phase diagram, see Supplemental Material [39]). For $-1.8 \lesssim J_z/t \lesssim -0.7$, the four lowest states (even, blue; odd, orange) are separated by a topological gap from a continuum of excited states. Black dash-dotted line, approximate analytical gap [39]. (b) Corresponding n_{holes} (green, diamonds) and total magnetization $|S_{\text{tot}}^z|$ (pink, stars). Dash-dotted lines, analytical results based on trial state. Fillings of symbols color coded as in (a). (c) Tunneling spectra at $J_z = -1.25t$ revealing zero-energy Majorana end states. (Parameters: $V = 2\Delta$, spin-orbit coupling $\alpha = 0.25$; a minute Zeeman field $B_z = 10^{-3}t$ singles out spin-polarized states in numerics and induces small intraparity splittings in ground-state manifold.)

zero-energy Majorana end states protected by a gap [Fig. 2(c)].

Discussion.—Dilute YSR chains constitute a versatile platform for quantum magnetism. Even for spin- $\frac{1}{2}$ adatoms, we uncover a rich phase diagram described by an extended $t - J$ model. Unlike the standard $t - J$ model, there are no restrictions on the sign of J nor on its strength relative to t . Tunneling spectra reflect its local spectral function, when accounting for additional pairing correlations.

Spin- $\frac{1}{2}$ impurities are directly realized for magnetic adatoms with one unpaired electron in the valence shell (e.g., cerium). Importantly, however, the relevant spin is not identical to the bare spin S_0 of the magnetic adatom on the superconducting substrate. Adatoms can bind a quasiparticle in any of the $2S_0$ conduction-electron channels [32]. The effective spin is thus equal to $S_0 - Q/2$, where Q denotes the number of bound quasiparticles, and the extended $t - J$ model can apply to higher-spin impurities, if all but one channel robustly bind a quasiparticle.

More generally, our results exemplify the importance of treating dilute YSR chains as quantum spin chains. Their effective spin depends on the detailed coupling between

adatom and substrate and can conceivably be tuned even for a given system, for instance, on gate-tunable superconductors [33] and on moiré [30] or charge-density-modulated [45,46] structures. The phenomenology of dilute YSR chains with higher spins is further refined by single-ion anisotropy as well as both intra- and interchannel YSR hybridization.

Unraveling the phenomenology of quantum YSR chains therefore promises important insights into the physics of magnetic adatoms on superconductors. While hybridizing subgap states form YSR bands in models with classical spin textures, we find that subgap spectra exhibit a plethora of qualitatively distinct behaviors depending on the magnetic phase. The quantum magnetism must also inform the search for topological superconductivity and Majorana zero modes in dilute YSR chains. In particular, we find that the parent metallic ferromagnet is limited in scope by competing insulating-ferromagnet and singlet-superconductor phases.

Finally, the physics of dilute YSR chains is not limited to magnetic adatoms, but can also be realized in chains of Coulomb-blockaded quantum dots coupled to a superconductor. Previous theoretical work focused on classical spins [47–49], but recent experiments on double quantum dots construct the elementary unit of quantum YSR chains [50,51]. When the quantum dots are tuned to odd Coulomb blockade islands, they realize $S = \frac{1}{2}$ spins, which can be coupled via a superconducting bulk. This provides a promising complement to recent work [52] on quantum dot arrays as quantum simulators of quantum magnetism.

We gratefully acknowledge funding through QuantERA grant TOPOQUANT and Deutsche Forschungsgemeinschaft through CRC 183 (project C03) as well as CRC 910.

[1] S. Nadj-Perge, I. K. Drozdov, B. A. Bernevig, and A. Yazdani, *Phys. Rev. B* **88**, 020407(R) (2013).
 [2] F. Pientka, L. I. Glazman, and F. von Oppen, *Phys. Rev. B* **88**, 155420 (2013).
 [3] D.-J. Choi, N. Lorente, J. Wiebe, K. von Bergmann, A. F. Otte, and A. J. Heinrich, *Rev. Mod. Phys.* **91**, 041001 (2019).
 [4] R. Pawlak, S. Hoffman, J. Klinovaja, D. Loss, and E. Meyer, *Prog. Part. Nucl. Phys.* **107**, 1 (2019).
 [5] K. Flensberg, F. von Oppen, and A. Stern, *Nat. Rev. Mater.* **6**, 944 (2021).
 [6] B. Jäck, Y. Xie, and A. Yazdani, [arXiv:2103.13210](https://arxiv.org/abs/2103.13210).
 [7] S. Nadj-Perge, I. K. Drozdov, J. Li, H. Chen, S. Jeon, J. Seo, A. H. MacDonald, B. A. Bernevig, and A. Yazdani, *Science* **346**, 602 (2014).
 [8] M. Ruby, F. Pientka, Y. Peng, F. von Oppen, B. W. Heinrich, and K. J. Franke, *Phys. Rev. Lett.* **115**, 197204 (2015).
 [9] R. Pawlak, M. Kisiel, J. Klinovaja, T. Meier, S. Kawai, T. Glatzel, D. Loss, and E. Meyer, *npj Quantum Inf.* **2**, 16035 (2016).

[10] B. E. Feldman, M. T. Randeria, J. Li, S. Jeon, Y. Xie, Z. Wang, I. K. Drozdov, B. Andrei Bernevig, and A. Yazdani, *Nat. Phys.* **13**, 286 (2017).
 [11] S. Jeon, Y. Xie, J. Li, Z. Wang, B. A. Bernevig, and A. Yazdani, *Science* **358**, 772 (2017).
 [12] H. Kim, A. Palacio-Morales, T. Posske, L. Rózsa, K. Palotás, L. Szunyogh, M. Thorwart, and R. Wiesendanger, *Sci. Adv.* **4**, eaar5251 (2018).
 [13] J. Li, H. Chen, I. K. Drozdov, A. Yazdani, B. A. Bernevig, and A. H. MacDonald, *Phys. Rev. B* **90**, 235433 (2014).
 [14] Y. Peng, F. Pientka, L. I. Glazman, and F. von Oppen, *Phys. Rev. Lett.* **114**, 106801 (2015).
 [15] L. Yu, *Acta Phys. Sin.* **21**, 75 (1965).
 [16] H. Shiba, *Prog. Theor. Phys.* **40**, 435 (1968).
 [17] A. I. Rusinov, *JETP Lett.* **9**, 85 (1969).
 [18] A. V. Balatsky, I. Vekhter, and J.-X. Zhu, *Rev. Mod. Phys.* **78**, 373 (2006).
 [19] K. Pöyhönen, A. Westström, J. Röntynen, and T. Ojanen, *Phys. Rev. B* **89**, 115109 (2014).
 [20] A. Heimes, P. Kotetes, and G. Schön, *Phys. Rev. B* **90**, 060507(R) (2014).
 [21] Y. Kim, M. Cheng, B. Bauer, R. M. Lutchyn, and S. Das Sarma, *Phys. Rev. B* **90**, 060401(R) (2014).
 [22] P. M. R. Brydon, S. Das Sarma, H.-Y. Hui, and J. D. Sau, *Phys. Rev. B* **91**, 064505 (2015).
 [23] S. Hoffman, J. Klinovaja, T. Meng, and D. Loss, *Phys. Rev. B* **92**, 125422 (2015).
 [24] M. Schechter, K. Flensberg, M. H. Christensen, B. M. Andersen, and J. Paaske, *Phys. Rev. B* **93**, 140503(R) (2016).
 [25] V. Kaladzhyan, C. Bena, and P. Simon, *Phys. Rev. B* **93**, 214514 (2016).
 [26] S. Körber, B. Trauzettel, and O. Kashuba, *Phys. Rev. B* **97**, 184503 (2018).
 [27] V. Madhavan, W. Chen, T. Jamneala, M. F. Crommie, and N. S. Wingreen, *Science* **280**, 567 (1998).
 [28] J. Li, W.-D. Schneider, R. Berndt, and B. Delley, *Phys. Rev. Lett.* **80**, 2893 (1998).
 [29] C. F. Hirjibehedin, C.-Y. Lin, A. F. Otte, M. Ternes, C. P. Lutz, B. A. Jones, and A. J. Heinrich, *Science* **317**, 1199 (2007).
 [30] K. J. Franke, G. Schulze, and J. I. Pascual, *Science* **332**, 940 (2011).
 [31] A. Sakurai, *Prog. Theor. Phys.* **44**, 1472 (1970).
 [32] F. von Oppen and K. J. Franke, *Phys. Rev. B* **103**, 205424 (2021).
 [33] E. J. Lee, X. Jiang, M. Houzet, R. Aguado, C. M. Lieber, and S. De Franceschi, *Nat. Nanotechnol.* **9**, 79 (2014).
 [34] L. Farinacci, G. Ahmadi, G. Reecht, M. Ruby, N. Bogdanoff, O. Peters, B. W. Heinrich, F. von Oppen, and K. J. Franke, *Phys. Rev. Lett.* **121**, 196803 (2018).
 [35] P. A. Lee, N. Nagaosa, and X.-G. Wen, *Rev. Mod. Phys.* **78**, 17 (2006).
 [36] R. Zitko, O. Bodensiek, and T. Pruschke, *Phys. Rev. B* **83**, 054512 (2011).
 [37] R. Zitko, M. Lee, R. López, R. Aguado, and M.-S. Choi, *Phys. Rev. Lett.* **105**, 116803 (2010).
 [38] N. Y. Yao, C. P. Moca, I. Weymann, J. D. Sau, M. D. Lukin, E. A. Demler, and G. Zaránd, *Phys. Rev. B* **90**, 241108(R) (2014).

- [39] See Supplementary Material at <http://link.aps.org/supplemental/10.1103/PhysRevLett.128.036801> for additional details of the analytical and numerical calculations.
- [40] A detailed discussion of the mapping is included in [39] to cover subtleties for periodic boundary conditions.
- [41] The small isolated regions near $J = 0$ are due to finite-size effects, which can be understood by noting that, for $J = 0$, Eq. (2) is an infinite- U Hubbard chain [39,42].
- [42] B. Douçot and X.G. Wen, *Phys. Rev. B* **40**, 2719 (1989).
- [43] We compute the physical spectral function of the Hamiltonian in Eq. (1), which incorporates anomalous correlators of the extended $t - J$ model, see [39] for details.
- [44] E. M. Stoudenmire, J. Alicea, O. A. Starykh, and M. P. A. Fisher, *Phys. Rev. B* **84**, 014503 (2011).
- [45] E. Liebhaber, S. Acero González, R. Baba, G. Reecht, B. W. Heinrich, S. Rohlf, K. Rossnagel, F. von Oppen, and K. J. Franke, *Nano Lett.* **20**, 339 (2020).
- [46] E. Liebhaber, L. Rütten, G. Reecht, J. Steiner, S. Rohlf, K. Rossnagel, F. von Oppen, and K. Franke, [arXiv:2107.06361](https://arxiv.org/abs/2107.06361).
- [47] T.-P. Choy, J. M. Edge, A. R. Akhmerov, and C. W. J. Beenakker, *Phys. Rev. B* **84**, 195442 (2011).
- [48] J. D. Sau and S. D. Sarma, *Nat. Commun.* **3**, 964 (2012).
- [49] I. C. Fulga, A. Haim, A. R. Akhmerov, and Y. Oreg, *New J. Phys.* **15**, 045020 (2013).
- [50] K. Grove-Rasmussen, G. Steffensen, A. Jellinggaard, M. H. Madsen, R. Žitko, J. Paaske, and J. Nygård, *Nat. Commun.* **9** (2018).
- [51] J. C. Estrada Saldaña, A. Vekris, R. Žitko, G. Steffensen, P. Krogstrup, J. Paaske, K. Grove-Rasmussen, and J. Nygård, *Phys. Rev. B* **102**, 195143 (2020).
- [52] J. P. Dehollain, U. Mukhopadhyay, V. P. Michal, Y. Wang, B. Wunsch, C. Reichl, W. Wegscheider, M. S. Rudner, E. Demler, and L. M. K. Vandersypen, *Nature (London)* **579**, 528 (2020).